

# The soft X-ray absorption lines of the Seyfert 1 galaxy MCG–6-30-15

A. K. Turner<sup>1\*</sup>, A. C. Fabian<sup>1</sup>, J. C. Lee<sup>2</sup> and S. Vaughan<sup>1,3</sup>

<sup>1</sup>Institute of Astronomy, Madingley Road, Cambridge CB3 0HA

<sup>2</sup>Chandra Fellow, Massachusetts Institute of Technology, Center for Space Research, 77 Massachusetts Ave. NE80, Cambridge, MA 02139, USA

<sup>3</sup>X-Ray and Observational Astronomy Group, Department of Physics and Astronomy, University of Leicester, Leicester, LE1 7RH

2 February 2008

## ABSTRACT

The absorption lines in the soft X-ray spectrum of MCG–6-30-15 are studied using the Reflection Grating Spectrometer data from the 2001 *XMM-Newton* 320 ks observation. A line search of the full time-averaged spectrum reveals 51 absorption lines and one emission line. The equivalent widths of the lines are measured and the majority of the lines identified. We find lines produced by a broad range of charge states for several elements, including almost all the charge states of oxygen and iron, suggesting a broad range of ionization parameters is present in the warm absorber. The equivalent widths of the lines are broadly consistent with the best fitting warm absorber models from Turner et al. (2003). The equivalent widths of the absorption lines allow confidence limits on the column density of the species to be determined. For O VII a column density of  $10^{18.36} - 10^{18.86} \text{ cm}^{-2}$  is found. This column density of O VII, when combined with the inferred Fe I absorption, is sufficient to explain the drop in flux at 0.7 keV as being due to absorption from the warm absorber. Fitting O I K-edge absorption to the spectrum reveals a column of  $10^{17.51} - 10^{17.67} \text{ cm}^{-2}$  of O I, suggesting an Fe:O ratio of  $\sim 1:2$ , consistent with the neutral iron being in the form of iron oxide dust. Variability is seen in a few absorption lines, but the majority of the absorption features, including the prominent absorption edges, stay constant throughout the observation despite variability in the continuum flux.

**Key words:** galaxies: active – galaxies: Seyfert: general – galaxies: individual: MCG–6-30-15 – X-ray: galaxies

## 1 INTRODUCTION

MCG–6-30-15 is a bright, nearby Seyfert 1 galaxy that shows many of the typical X-ray spectral features found in other Seyfert 1s. The X-ray spectrum consists of a power-law continuum with  $\Gamma \sim 1.9$ , broad iron K $\alpha$  emission line and a soft excess (e.g. Fabian et al. 2002). The spectrum of MCG–6-30-15 also shows a sharp drop in flux at  $\sim 0.7$  keV. In the pre-*Chandra/XMM-Newton* era, this drop was interpreted as being due to O VII and O VIII K-shell edges from ionized gas in the environment of the AGN (“the warm absorber”; Otani et al. 1996; Reynolds 1997; George et al. 1998).

This interpretation of the drop in flux at 0.7 keV was challenged by Branduardi-Raymont et al. (2001), using a  $\sim 120$  ks Reflection Grating Spectrometer (RGS) *XMM-Newton* observation. They explain the drop as the blue wing of a broad O VIII emission line. The broadening mechanism of the line was taken to be the same relativistic blurring that produces a broad iron line at  $\sim 6$  keV. Part of the reason for adopting such a model was an apparent  $\sim 16,000 \text{ km s}^{-1}$  discrepancy in the position of the drop in flux and the energy of the O VII edge (0.74 keV). Smaller drops

at  $\sim 0.39$  and  $\sim 0.54$  keV were similarly explained as being due to emission from C VI and N VII respectively.

Lee et al. (2001) countered these claims with yet higher spectral resolution High Energy Transmission Grating Spectrometer (HETGS) observations taken with *Chandra*. This discrepancy was interpreted by Lee et al. (2001) to be due to the presence of an Fe I L-shell absorption edge at the 0.7 keV drop, which when combined with O VII resonance absorption lines and edge could adequately explain the drop in flux at 0.7 keV. Lee et al. (2001) concluded the Fe I could be in the form of dust embedded in the warm absorber (the Dusty Warm Absorber, DWA), either in the form of iron oxides or silicates, which would explain the optical observations of Reynolds et al. (1997) where  $E(V - B)$  reddening suggests strong dust extinction is present (see Ballantyne et al. (2003) for a discussion of the location of the dust).

Sako et al. (2003), however, fitted the DWA model of Lee et al. (2001) and the Relativistic Emission Line (REL) model of Branduardi-Raymont et al. (2001) to the *XMM-Newton* RGS observation and claimed that the REL model provides a much better fit to the data than the DWA model. Models of absorption by various species were also fitted to the absorption lines seen in the data. Sako et al. (2003) claimed that the column densities of O VII and

\* E-mail: akt21@ast.cam.ac.uk

O VIII, derived from the observed absorption lines, are insufficient to explain the 0.7 keV drop by absorption.

MCG–6–30–15 was observed for a further three *XMM-Newton* revolutions in 2001, providing 320 ks of data when the source was at a higher flux level (Fabian et al. 2002) than the previous *XMM-Newton* observation reported by Branduardi-Raymont et al. (2001) and Sako et al. (2003). An analysis of the RGS spectrum unambiguously showed the presence of Fe I through the absorption fine structure at the L-shell edge (Turner et al. 2003). The 0.7 keV drop could also be adequately fitted by Fe I and O VII absorption. Self-consistent models of warm absorption were made using the photoionization code CLOUDY and fitted to the data along with the REL model. Both models provided similar quality fits to the data and both were capable of explaining the gross features of the spectrum. The DWA model was, however, more physically self-consistent, since the REL model requires the underlying continuum to be very flat below  $\sim 1$  keV and steep above this energy. Conventional models of Seyfert 1 emission do not contain such a break. Moreover, the predicted equivalent widths of the emission lines of the REL model in Branduardi-Raymont et al. (2001), Sako et al. (2003) and Turner et al. (2003) were much larger than the largest equivalent widths predicted by ionized disc models and also lacked the iron L emission predicted by those same models (e.g. Ballantyne et al. 2002; Różańska et al. 2002).

MCG–6–30–15 also shows interesting spectral variability: The flux in the iron K $\alpha$  line is observed to stay constant while the flux in the continuum varies (Lee et al. 2000; Vaughan & Edelson 2001; Lee et al. 2002; Shih, Iwasawa, & Fabian 2002; Fabian et al. 2002). If a spectrum from a low flux period is subtracted from a spectrum from a high flux period then the resulting spectrum is adequately fitted by a power-law (Fabian et al. 2002). These properties led Fabian & Vaughan (2003) to propose a two component model for the emission in MCG–6–30–15 consisting of a varying power-law component and an almost constant reflection dominated component. This differencing method was used by Turner et al. (2003) to remove the effects of absorption from the 320 ks RGS observation and determine the underlying continuum. It shows that the spectrum does not contain any strong relativistic emission lines and confirms that absorption is responsible for the 0.7 keV drop.

In this paper we use the absorption lines seen in the RGS spectrum from the 320 ks *XMM-Newton* observation to measure the parameters of individual species that make up the warm absorber. We do not assume a continuum, either DWA or REL, but instead use a cubic spline fit to determine the flux level around the absorption lines. This way the absorption line parameters can be determined without any prior assumption being made about which model is correct. This information is used to confirm that a DWA model accounts for the observed spectral features, specifically the drop in flux at 0.7 keV. The paper is organised as follows: Section 2 describes the method used to find, identify and measure the absorption lines as well as the results obtained by this method. In section 4 the evidence for the presence and composition of dust is examined. In section 5 the variability of the absorption lines is measured. In section 6 the results are discussed.

## 2 ABSORPTION LINE PROPERTIES

### 2.1 Observations and data reduction

We observed MCG–6–30–15 with *XMM-Newton* on 2001 July 31 to 2001 August 5 (revolutions 301, 302 and 303) for  $\sim 320$  ks

(Fabian et al. 2002). The Observation Data Files (ODFs) were analysed using the standard reduction chains provided by the 5.4.1 release of the *XMM-Newton* Science Analysis Software (SAS V5.4.1) and the associated calibration files. The last few ks of each orbit data were removed since these periods showed strong background flaring. The final RGS spectra were rebinned so at least 20 counts were present in each spectral bin and were fitted to trial models in the X-ray spectral fitting package XSPEC V11.2 (Arnaud 1996).

The previous *XMM-Newton* observation of MCG–6–30–15 was taken on 2000 July 10–11 and consists of  $\sim 120$  ks of data (Branduardi-Raymont et al. 2001). It was reduced using the same prescription as described above.

### 2.2 Line finding

To determine the presence of any spectral absorption lines, the spectra were divided up into a number of regions, each region being analysed separately. The regions were chosen so they did not span any of the large drops in flux and contained approximately the same number of spectral bins (the regions are shown as individual panels in Fig. 1). The exception to this was the 0.534–0.714 keV region which spans the Fe I edge at 0.702 keV. This was done to allow the O VII  $1s^2 - 1s5p$  line to be included in the same region as the other O VII  $1s^2 - 1snp$  lines. In this case a model of Fe I absorption was included (Turner et al. 2003). Within each region the spectra were fitted with a power-law, Galactic absorption ( $N_H = 4.06 \times 10^{20} \text{ cm}^{-2}$ ; Elvis, Wilkes, & Lockman 1989) and an additional multiplicative model component to account for any unknown variations in the underlying continuum either from complexity in the underlying continuum or weak photoelectric edges. A cubic spline function with a number of knots evenly separated in energy across the region was chosen for this additional component (Press et al. 1999). The number of knots varied between 5 and 10 depending on the relative size of the region to the FWHM of the line spread function. A model absorption line (with Gaussian opacity profile) was then fitted with fixed energy to the data at regular intervals across the region. The separation between points where the line was fitted was made to be less than the FWHM of the instrumental response to ensure that no significant lines were missed. Once the line had been moved across the region it was fitted with its energy free to vary to the point where the presence of the line improved the  $\chi^2$  of the fit the most. The significance of the improvement in  $\chi^2$  upon adding this line was assessed using the F-test and a 95 per cent confidence limit. If the line was found to be significant then the line position was recorded and the region around this line was removed (within 1 instrumental FWHM either side of the line centre). The process was repeated until no more points produced significant improvements in the fit. The process produced a list of 51 lines whose positions span the whole RGS passband (see Table 1). Because of the significance level used above, a few of the weaker found lines may be spurious detections.

### 2.3 Line parameter determination

Once the positions of the significant lines had been determined, the equivalent widths of these lines were determined. To determine the equivalent widths, the regions of the spectra were again individually fitted to a power-law, Galactic absorption and cubic spline (and Fe I in the case of the 0.534–0.713 keV region). Then absorption line models were placed at the energies found in section 2.2 and fitted to the data.

It was decided to use a simple notch model for the line model rather than the more complicated Gaussian opacity profile model used in Section 2.2. A notch model is an absorption model in which the transmission is zero within the line width and unity outside. The XSPEC fitting package convolves this absorption model with the instrumental response before fitting it to the data. It was found that this notch model could be adequately fitted to the data for all but one of the line positions<sup>1</sup>. This suggests that the widths of the absorption lines are less than the width of the instrumental line spread function. The notch model has the advantage that its width gives a direct measurement of the equivalent width of the absorption line and so error determination on the equivalent width is more straightforward. It also provides a good approximate model for an absorption line lying on the saturated (flat) part of the curve of growth. The accuracy of this model at reproducing absorption lines that have been convolved with the instrumental line spread function was tested. The model was found to accurately reproduce the profile shape for a broad range of line parameters.

The best fits to the regions have reduced  $\chi^2$  values of  $\sim 1.1$ . The best fitting continuum model does not represent the true emission from the central source as the amount of continuum absorption from photoelectric edges at any given point in the spectrum is unknown. Also the details of reflection spectra are highly uncertain and any attempt to introduce a self-consistent model of the continuum will result in the continuum level being at the incorrect level for many of the lines. The purpose of this work is to measure the absorption line properties without assuming any physical continuum, either of the DWA or REL type. The continuum model here represents the flux level to either side of the narrow absorption lines and allows the equivalent width of those lines to be measured.

The errors on the equivalent widths of the lines were determined using a standard  $\Delta\chi^2 = 1.0$  criterion. Due to the corrugated nature of the  $\chi^2$  space with respect to line position, a Monte Carlo technique was used to determine the line position error and avoid problems with the XSPEC error command. The number of counts in each spectral bin in the source and background spectra were perturbed by a Poisson distribution with mean counts equal to the source and background count rate respectively. The best fitting line model was then fitted to this new spectra and the resulting best fitting parameters recorded. This was repeated 1000 times and the resulting distribution of parameters used to determine the error.

The best fitting line models are shown compared to the combined and fluxed spectrum from all three orbits in Fig. 1 and the derived line parameters are given in Table 1. Also found during the fitting was a narrow emission feature at 0.5565 keV with an equivalent width of  $0.777 \pm 0.238$  eV and is identified as O VII forbidden emission. The line finding method of section 2.2 is only able to find the highest equivalent width lines due to the presence of noise in the data. Therefore, when the continuum and line model is fitted to the data, the continuum component will be below the true level, since it is actually fitting to the average level of the continuum plus the undetected, low equivalent width lines. Since the model continuum is below the true continuum the equivalent widths of the model lines will be underpredicted in general. The use of a many knot cubic spline to model the continuum means that only those missed lines near a found line affect its equivalent width rather than an average of all the missed lines in the region. Unresolved blends of many lines will also be missed and filled in by the spline

continuum. This is true for the iron Unresolved Transition Array (UTA, e.g. Sako et al. 2001; Behar et al. 2001) which has the effect of lowering the continuum between  $\sim 0.7$  and  $\sim 0.8$  keV.

## 2.4 Line identification

The lines were identified by comparing their positions to the energies quoted in several atomic data sources for the positions of known absorption transitions. Those sources used were Verner et al. (1996), the NIST<sup>2</sup> database and the line lists from the CLOUDY<sup>3</sup>, PHOTOION<sup>4</sup> and XSTAR<sup>5</sup> photoionization codes. For inner-shell transitions McLaughlin & Kirby (1998), Behar & Netzer (2002), Behar & Kahn (2002) and Pradhan et al. (2003) were used. Although Verner et al. (1996) provides the most accurate data (it only includes transition energies that have been experimentally verified) it does not include many important transitions. One example of this is for the highest oscillator strength line of Fe XIX which is not present in the Verner et al. (1996) list. The positions for this line in the NIST, CLOUDY, PHOTOION and XSTAR line lists are 0.9170, 0.9211, 0.9170 and 0.9030 keV respectively. Such variation in energy and the lack of a complete and accurate line list makes the correct identification of the observed lines difficult.

In order to identify the observed lines, the transition with the largest oscillator strength from each of the species considered was compared to the positions of the observed lines. The species considered were C V-VI, N V-VII, O I-VIII, Ne II-IX, Si X-XII, S X-XIV, Ar IX-XVI and Fe XVI-XXIV. Since there is such a large variation in the theoretical line positions between the atomic data sets, the transition positions from each atomic data set were compared simultaneously. If an observed line was close to the transition from the data sets and it was reasonable to expect to see it (the transition had a high oscillator strength and the element has high cosmic abundance or the transition had been seen in other sources) then the identification was made. Once the highest oscillator strength line of a particular species had been identified, the search proceeded for the lines of the same species in order of decreasing oscillator strength. If a transition could not be found then any transitions with a lower oscillator strength from the same species were not identified. The exception to this rule was C V where the  $1s^2 - 1snp$  with  $n = 3, 4, 5$  lines could be clearly identified and are expected and the  $1s^2 - 1s2p$  line would have its location in a confused part of the spectrum at 0.3518 keV. No reliable atomic data exists for the inner shell transitions of nitrogen although they are predicted to occur in the DWA models of Turner et al. (2003). Some of the unidentified transitions around 0.42 keV may be due to these transitions.

Lines from a broad range of ionization states were identified in the data. Oxygen and iron states are the most numerous with detections of almost all species of oxygen and iron species from Fe XVII to Fe XXIV, as well as Fe I from the L-edge and Fe II to Fe XVI from the UTA (Turner et al. 2003). At energies below  $\sim 0.5$  keV absorption lines of carbon and nitrogen are significant. A broad range of neon species are also detected from Ne V to Ne X including several inner-shell transitions. A careful examination of the data shows that several transitions may have been missed because of chip gaps and other problems in the instrumental responses. There

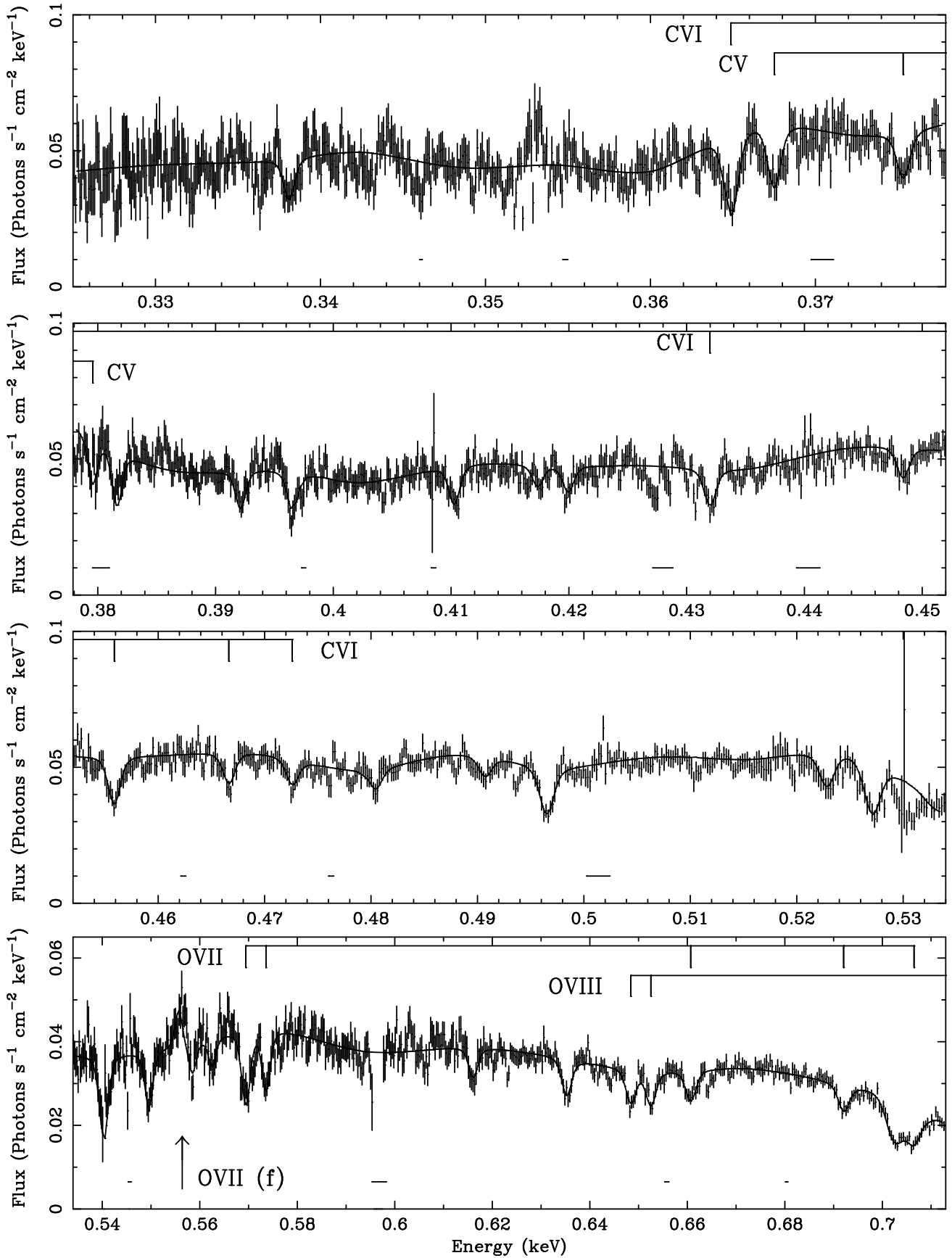
<sup>1</sup> This line (line 43) was fitted with a model line with a Gaussian opacity profile. The width of the line was determined to be  $1870 \pm 220$  km s<sup>-1</sup>.

<sup>2</sup> [http://physics.nist.gov/cgi-bin/AtData/main\\_asd](http://physics.nist.gov/cgi-bin/AtData/main_asd)

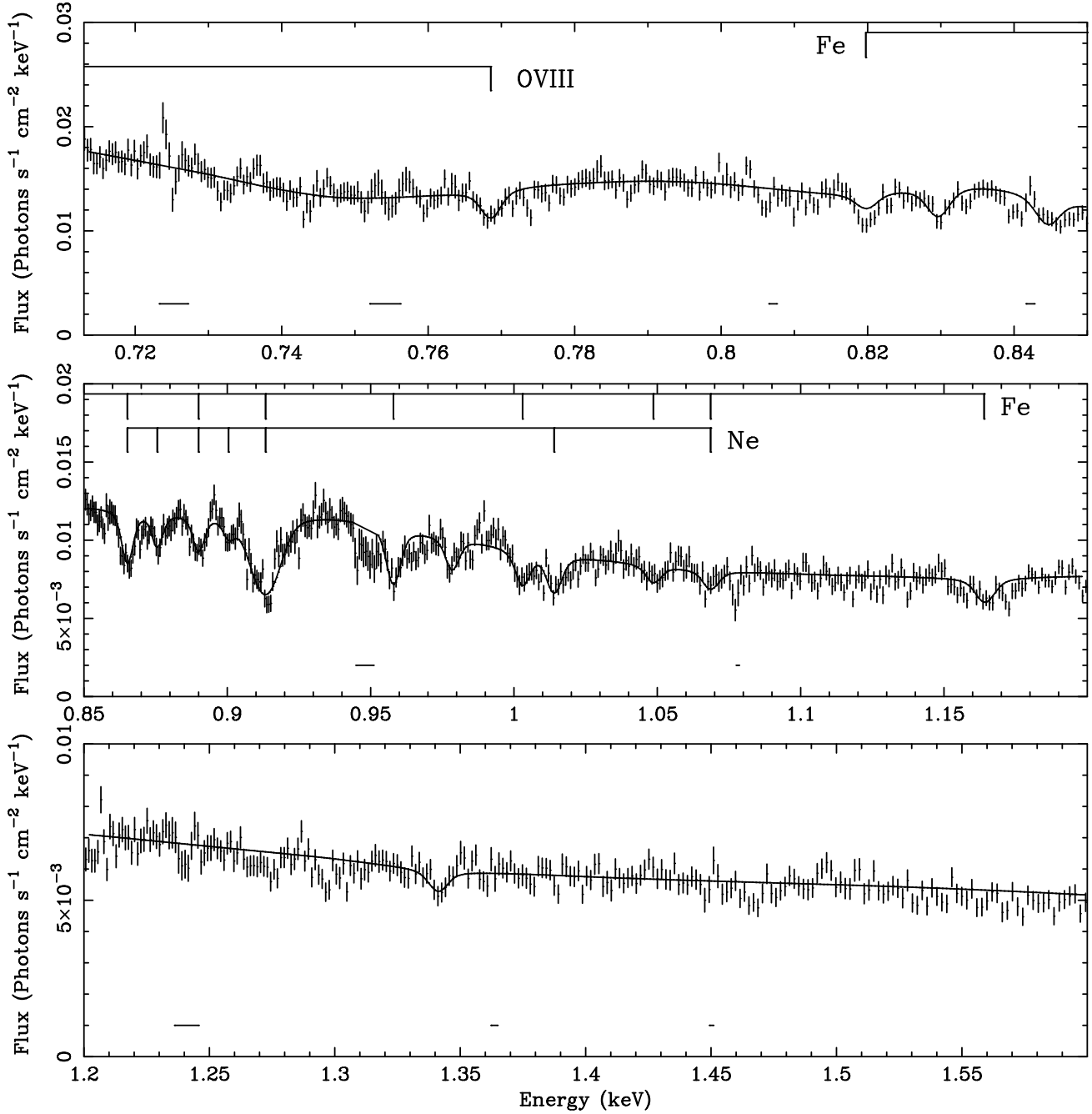
<sup>3</sup> <http://www.nublado.org>

<sup>4</sup> <http://xmm.astro.columbia.edu/photoion/photoion.html>

<sup>5</sup> <http://heasarc.gsfc.nasa.gov/docs/software/xstar/xstar.html>



**Figure 1.** Best fitting line model compared to fluxed and combined RGS spectrum. The lines below the spectrum indicate the positions of chip-gaps and other poor quality regions in the detectors. The line labels above the spectrum indicate the positions of the lines for several species. Also labelled is the O VII forbidden emission line at 0.5565 keV.

Figure 1. *Continued*

appears to be a line directly over a chip gap at 0.427 keV which fits the position of N VI. Another line appears to exist at 0.5306 keV, whose position matches the position of O III. If this line is due to O III then every species of oxygen is evident in the spectrum suggesting a broad range of ionization parameters is present in the warm absorber. Two velocity zones are identified, as was found in Sako et al. (2003). One has a velocity of  $80 \pm 260 \text{ km s}^{-1}$  and the other  $-1970 \pm 160 \text{ km s}^{-1}$ , where the errors are calculated from the variance of the individual velocity values for the lines. Only two lines (O VII  $1s^2 - 1s2p$  and O VIII Ly $\alpha$ ) are identified with the second, outflowing, zone. Although not all the observed lines have identifications some of these may be random Poisson fluctuations in the data rather than true lines.

### 3 WARM ABSORBER PROPERTIES

#### 3.1 Confidence region determination

In Section 2.3 the equivalent widths of the lines were measured in an independent way with no reference to which species might be causing those lines or assumptions about the underlying continuum. Now that those lines have been identified we can use those equivalent widths, combined with a knowledge of the atomic parameters of those lines, to calculate confidence regions for the turbulent velocity of the species and its absorbing column density towards the central source of X-rays. The profile of an absorption line which has been Doppler broadened is given by the convolution of a Lorentzian profile (caused by radiation damping) and a

**Table 1.** Table showing lines found in the spectra with measured energies, wavelengths, equivalent widths and identifications where they have been made. For lines with identifications the rest frame energy and its reference are shown (for these identification in brackets if more than one is present for a single line), as well as, the velocity relative to the frame of MCG-6-30-15. Reference key: 1: Verner et al. (1996), 2: Behar & Netzer (2002), 3: Pradhan et al. (2003), 4: McLaughlin & Kirby (1998).

No.	Energy keV	Wavelength Å	EW eV	Identification	Rest Energy keV	Reference	Velocity km s <sup>-1</sup>
1	0.338090 ± 0.000095	36.672 ± 0.010	0.372 ± 0.070				
2	0.364880 ± 0.000076	33.9794 ± 0.0071	0.749 ± 0.071	C VI Lyα	0.367517	1	-157 ± 63
3	0.36751 ± 0.00012	33.736 ± 0.011	0.498 ± 0.059	C V 1s <sup>2</sup> - 1s4p	0.370923	1	461 ± 96
4	0.37532 ± 0.00011	33.034 ± 0.010	0.407 ± 0.060	C V 1s <sup>2</sup> - 1s5p	0.378533	1	243 ± 92
5	0.37957 ± 0.00017	32.664 ± 0.014	0.399 ± 0.092	C V 1s <sup>2</sup> - 1s6p	0.382673	1	124 ± 133
6	0.381635 ± 0.000088	32.4876 ± 0.0075	0.547 ± 0.075	S XIII 2s <sup>2</sup> - 2s3p	0.384546	1	-37 ± 70
7	0.39213 ± 0.00010	31.6185 ± 0.0082	0.433 ± 0.071	Ar XII	0.395210	1	34 ± 79
8	0.39654 ± 0.00011	31.2668 ± 0.0085	0.469 ± 0.087	Si XII	0.399752	1	108 ± 82
9	0.41028 ± 0.000096	30.2198 ± 0.0071	0.461 ± 0.072				
10	0.41735 ± 0.00046	29.707 ± 0.033	0.260 ± 0.075				
11	0.41995 ± 0.00024	29.524 ± 0.017	0.321 ± 0.073				
12	0.431980 ± 0.000081	28.7014 ± 0.0054	0.511 ± 0.064	C VI Lyβ	0.435562	1	164 ± 58
13	0.44843 ± 0.00013	27.6486 ± 0.0081	0.452 ± 0.071				
14	0.455880 ± 0.000074	27.1967 ± 0.0044	0.602 ± 0.060	C VI Lyγ	0.459379	1	-22 ± 49
15	0.466640 ± 0.000093	26.5696 ± 0.0053	0.408 ± 0.058	C VI Lyδ	0.470402	1	94 ± 60
16	0.47260 ± 0.00014	26.2345 ± 0.0076	0.339 ± 0.062	C VI Lyε	0.476391	1	81 ± 88
17	0.48048 ± 0.00015	25.8042 ± 0.0082	0.316 ± 0.078				
18	0.49072 ± 0.00028	25.266 ± 0.014	0.284 ± 0.063	Ar XII	0.495149	1	382 ± 170
19	0.496510 ± 0.000064	24.9711 ± 0.0032	0.806 ± 0.066	N VII Lyα	0.500324	1	-21 ± 39
20	0.52284 ± 0.00012	23.7136 ± 0.0055	0.594 ± 0.093	O I	0.526790	4	-58 ± 70
21	0.52704 ± 0.00010	23.5246 ± 0.0046	0.934 ± 0.099	O II	0.531893	3	437 ± 59
22	0.54035 ± 0.00013	22.9452 ± 0.0056	1.67 ± 0.14	O IV	0.544507	3	-17 ± 74
23	0.54959 ± 0.00013	22.5594 ± 0.0053	1.123 ± 0.097	O V	0.553996	3	80 ± 71
24	0.558430 ± 0.00127	22.202 ± 0.051	0.652 ± 0.086	O VI KLL	0.562287	3	-253 ± 689
25	0.56255 ± 0.00017	22.0397 ± 0.0065	0.578 ± 0.091	O VI KLL	0.567433	3	279 ± 89
26	0.56944 ± 0.00013	21.7730 ± 0.0051	1.140 ± 0.091	O VII 1s <sup>2</sup> - 1s2p	0.573956	1	54 ± 71
27	0.57358 ± 0.00013	21.6159 ± 0.0047	1.006 ± 0.089	O VII 1s <sup>2</sup> - 1s2p	0.573956	1	-2127 ± 65
28	0.61606 ± 0.00016	20.1253 ± 0.0052	0.62 ± 0.10	O V			
29	0.635260 ± 0.000092	19.5171 ± 0.0028	0.892 ± 0.067	O VI			
30	0.64840 ± 0.00011	19.1216 ± 0.0031	0.910 ± 0.077	O VIII Lyα	0.653625	1	92 ± 49
31	0.65252 ± 0.00012	19.0008 ± 0.0036	0.950 ± 0.076	O VIII Lyα	0.653625	1	-1816 ± 57
32	0.66070 ± 0.00021	18.7656 ± 0.0059	0.876 ± 0.086	O VII 1s <sup>2</sup> - 1s3p	0.665558	1	-119 ± 95
33	0.69205 ± 0.00020	17.9155 ± 0.0053	0.942 ± 0.087	O VII 1s <sup>2</sup> - 1s4p	0.697802	1	168 ± 89
34	0.70651 ± 0.00017	17.5488 ± 0.0043	1.11 ± 0.12	O VII 1s <sup>2</sup> - 1s5p	0.712724	1	313 ± 74
35	0.76855 ± 0.00035	16.1322 ± 0.0073	1.04 ± 0.19	O VIII Lyβ	0.774623	1	46 ± 138
36	0.81975 ± 0.00042	15.1245 ± 0.0077	0.71 ± 0.22	Fe XVII			
37	0.82959 ± 0.00034	14.9452 ± 0.0061	1.19 ± 0.21				
38	0.84465 ± 0.00043	14.6788 ± 0.0075	1.418 ± 0.021				
39	0.86513 ± 0.00037	14.3313 ± 0.0061	2.12 ± 0.21	Fe XVIII, (Ne V)	0.870740	2	-379 ± 129
40	0.87559 ± 0.00053	14.1601 ± 0.0086	1.31 ± 0.20	Ne VI	0.884340	2	673 ± 183
41	0.89000 ± 0.00050	13.9308 ± 0.0077	1.54 ± 0.20	Fe XIX, (Ne VII)	0.897530	2	213 ± 167
42	0.90043 ± 0.00053	13.7694 ± 0.0081	0.76 ± 0.22	Ne VIII	0.908580	2	390 ± 178
43	0.91337 ± 0.00043	13.5744 ± 0.0065	7.63 ± 0.84	Fe XIX, (Ne IX)	0.922023	1	518 ± 144
44	0.95794 ± 0.00050	12.9427 ± 0.0068	3.46 ± 0.32	Fe XX			
45	0.97841 ± 0.00063	12.6720 ± 0.0082	2.06 ± 0.33				
46	1.00300 ± 0.00078	12.3613 ± 0.0096	2.47 ± 0.38	Fe XXI			
47	1.0140 ± 0.0011	12.227 ± 0.013	2.88 ± 0.40	Ne X Lyα	1.021810	1	-14 ± 321
48	1.0486 ± 0.0012	11.824 ± 0.013	1.49 ± 0.44	Fe XXII			
49	1.0686 ± 0.0017	11.602 ± 0.018	1.81 ± 0.45	Fe XXIII, (Ne IX)	1.073783	1	-869 ± 477
50	1.1640 ± 0.0032	10.652 ± 0.029	3.21 ± 0.58	Fe XXIV			
51	1.34100 ± 0.00095	9.2457 ± 0.0065	2.31 ± 0.51	Mg XI 1s <sup>2</sup> - 1s2p	1.352253	1	192 ± 214

Gaussian profile (from Doppler broadening) giving the Voigt profile. The Doppler broadening is caused by a combination of thermal broadening and turbulent broadening, with turbulent broadening being the dominant mechanism for the gas within the single zone warm absorber (Nicastro et al. 1999). The nature of the Voigt profile means that for a single line turbulent velocity and col-

umn density are highly degenerate. To break this degeneracy several other lines from the same species are required or upper limits for the equivalent widths if no other lines are positively identified. Having more than one line for a species, therefore, allows tighter constraints to be placed on the column density and turbulent velocity than would otherwise be the case. For instance, if the O VII

$1s^2 - 1s2p$  line is considered on its own the column density is only constrained to lie in the range  $\sim 10^{16.5} - 10^{18.8} \text{ cm}^{-2}$  and the turbulent velocity is unconstrained in the  $10 - 350 \text{ km s}^{-1}$  range. The expected equivalent width of a line given a particular turbulent velocity and column density can be found by numerically integrating the absorbed area under the normalised Voigt profile. Confidence regions for the turbulent velocity and column density of a particular species were determined by calculating the expected equivalent widths for all the observed lines of that species across a grid of turbulent velocity and column density values. These values were then compared to the observed equivalent widths and errors calculated in section 2.3 to produce a grid of  $\chi^2$  values. By drawing contours at particular values of  $\chi^2$  confidence regions could be calculated. The atomic data used to calculate the Voigt profiles was from Verner et al. (1996), the same source of atomic data used by Sako et al. (2003).

This method can be checked by replacing the notch models with Voigt profiles for the lines of interest (constraining the column density and turbulent velocity to be the same for all of the lines) and fitting to the data. Confidence regions are then obtained by calculating the  $\Delta\chi^2$  from the best fit for a grid of column density and turbulent velocity.

### 3.2 Results

#### 3.2.1 Oxygen

O VII is a prime candidate for analysis since four lines in the first velocity zone are identified ( $1s^2 - 1snp$ ,  $n = 2, 3, 4, 5$ ) in a region of the spectrum with high signal to noise. The confidence region for turbulent velocity and column density considering all four lines is shown in Fig. 2. The column density of O VII in the first velocity zone is shown to lie in the region  $10^{18.36} - 10^{18.64} \text{ cm}^{-2}$  and the turbulent velocity in the range  $86 - 99 \text{ km s}^{-1}$  with  $1\sigma$ . The implied optical depth of the O VII edge is 0.57 (taking the lower  $1\sigma$  bound of the column density) suggesting that O VII absorption is responsible for the majority of the drop at 0.7 keV as predicted by the DWA model. This column density places the  $1s^2 - 1snp$ ,  $n = 2, 3, 4, 5$  lines on the saturated part of the curve of growth. The result was confirmed by fitting Voigt profiles directly to the data (see section 3.1 and Fig. 3). As mentioned by Sako et al. (2003) the presence of O VII forbidden emission suggests that the O VII  $1s^2 - 1s2p$  may be partially filled in by resonance emission. To take this into account the prescription of Sako et al. (2003) was used where the ratio of forbidden to resonance emission is fixed at a value of 3 for a recombination-dominated plasma. One other issue is that the  $1s^2 - 1s5p$  transition lies over the position of the Fe I  $L_3$  edge for Galactic absorption. By calculating the equivalent width of the line-like feature at the edge energy of Fe I this can be taken into account. By taking the limit of the confidence regions from all the various combinations of corrections a more robust confidence region is obtained. This produces a  $1\sigma$  confidence limit on the column density of  $10^{18.36} - 10^{18.86} \text{ cm}^{-2}$  and turbulent velocity of  $79 - 100 \text{ km s}^{-1}$ . If a similar analysis is performed for O VIII then  $1\sigma$  confidence limits for column density of  $10^{17.42} - 10^{18.47} \text{ cm}^{-2}$  and for turbulent velocity of  $46 - 111 \text{ km s}^{-1}$  are obtained.

The O VII column density limit obtained above is much larger than that obtained by Sako et al. (2003) using the earlier *XMM-Newton* observation. To investigate this issue the 2000 *XMM-Newton* observation was analysed using the method described above. The best fitting model from the 2001 data was used but the line and continuum parameters were allowed to vary. Equivalent

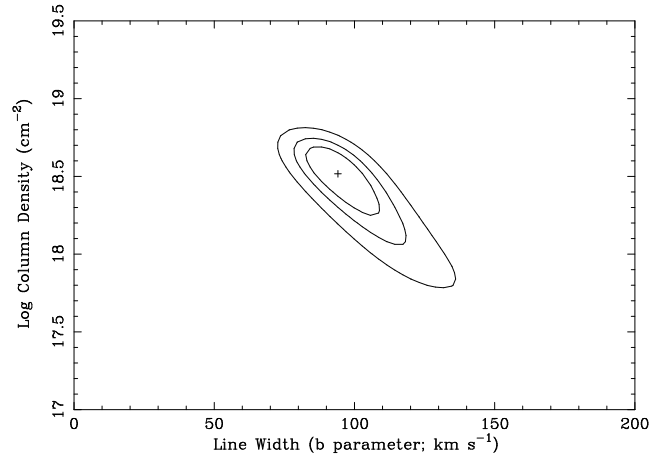


**Figure 2.** Confidence region for column density and turbulent velocity for O VII using measured equivalent widths of the O VII  $1s^2 - 1snp$ ,  $n = 2, 3, 4, 5$  absorption lines.

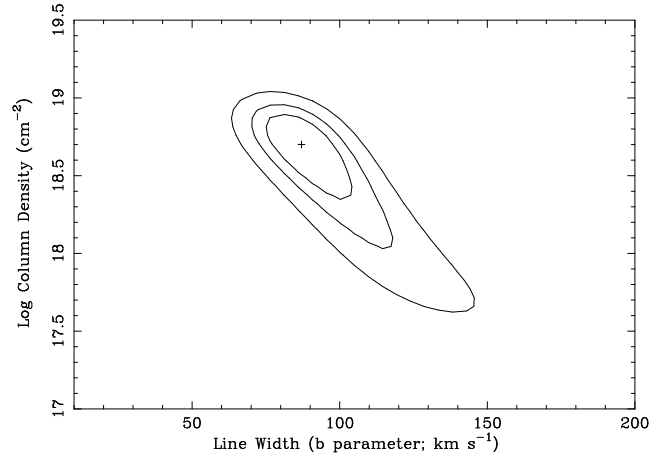


**Figure 3.** Confidence region for column density and turbulent velocity for O VII determined by fitting Voigt profiles to the O VII  $1s^2 - 1snp$ ,  $n = 2, 3, 4, 5$  absorption lines.

widths and errors for the O VII  $1s^2 - 1snp$ ,  $n = 2, 3, 4, 5$  lines were measured as above and used to determine a confidence region for column density and turbulent velocity for the 2000 data. This is shown in Fig. 4 and is compared to the limits found by Sako et al. (2003) and in this paper for the 2001 data. The contours overlap the 2001 contours (which are much smaller because of the higher signal-to-noise of the 2001 observation) but do not overlap the contours found by Sako et al. (2003). An examination of the equivalent width obtained for the O VII  $1s^2 - 1s2p$  line reveals a significant difference between that found here ( $1.14 \text{ eV}$ ,  $44 \text{ mÅ}$ ) and that found by Sako et al. (2003) ( $0.48 \text{ eV}$ ,  $18 \text{ mÅ}$ ). We are unable to account for this difference. The region around the O VII  $1s^2 - 1s2p$  line is shown in Fig. 5. Also shown is the best fitting model from Section 2.3, as well as this model with the O VII  $1s^2 - 1s2p$  line with the equivalent width expected using the column density and turbulent velocity of O VII determined in Sako et al. (2003). This equivalent width also includes the expected response emission infilling. Clearly the Sako et al. (2003) values of column density and turbulent velocity under-predict the equivalent width of the line.

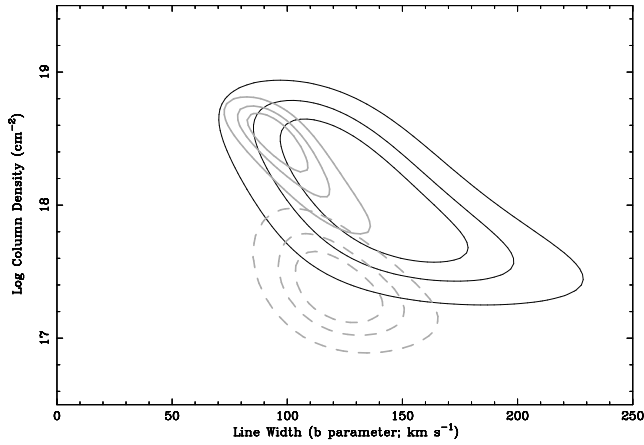


**Figure 4.** Confidence regions for column density and turbulent velocity for O VII. (*black*): This paper's analysis using the 2000 data. (*solid grey*): This paper's analysis using the 2001 data. (*dashed grey*): Sako et al. (2003) analysis using the 2000 data.

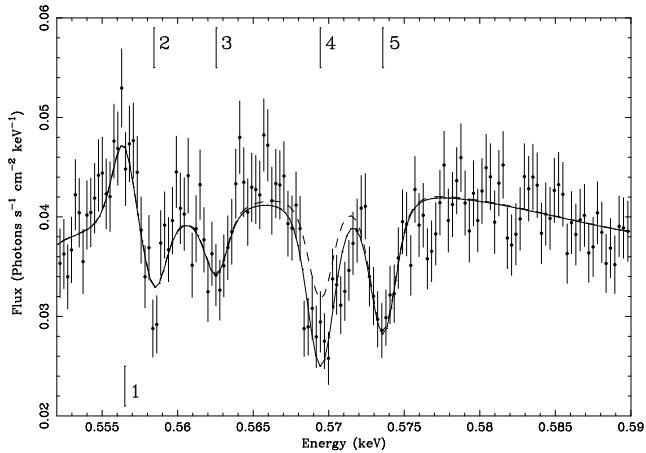


**Figure 5.** Detail of spectrum around the O VII  $1s - 2p$  line. Overlaid is the best fitting model from Section 2.3 (*solid*) as well as this best fitting model with the equivalent width of O VII  $1s - 2p$  for the column density and turbulent velocity from Sako et al. (2003) (*dashed*). Also labelled are (1) the O VII forbidden emission line, (2,3) the O VI KLL lines, (4) the O VII  $1s - 2p$  line for the first velocity zone and (5) the O VII  $1s - 2p$  line for the second velocity zone.

### 3.2.2 Carbon

C VI has five identified lines ( $1s - np$ ,  $n = 2, 3, 4, 5, 6$ ). Calculating the confidence region for this species produces a poor fit and two separate  $\chi^2$  minima because the  $n = 3$  line has a lower equivalent width than the  $n = 4$  line when it should have a larger equivalent width due to its higher oscillator strength. There are two possibilities to explain this: either the  $n = 3$  is underpredicted (because unidentified low equivalent width lines nearby mean the fitted continuum is lower than the true continuum) or the  $n = 4$  transition is blended with another transition (so increasing its apparent equivalent width). Since no other transition can be found that fits the position of the  $n = 4$  transition the former explanation is favoured. Removing the  $n = 3$  line from the analysis results in a single minimum in the confidence region with column density lying in the range  $10^{16.46} - 10^{16.77} \text{ cm}^{-2}$  and turbulent velocity in the range  $122 - 153 \text{ km s}^{-1}$  ( $1\sigma$  confidence limit). Because no measurement is

**Table 2.** Comparison of column densities ( $N_X$ ) and turbulent velocities ( $V_{\text{turb}}$ ) between this work and DWA models in Turner et al. (2003).  $N_X$  is given in units of  $\log \text{ cm}^{-2}$  and  $V_{\text{turb}}$  in units of  $\text{km s}^{-1}$ . The DWA models in Turner et al. (2003) assumed a  $V_{\text{turb}}$  of  $100 \text{ km s}^{-1}$ .

Species	DWA models			This work	
	1	2	3	$\log N_X$ $\text{cm}^{-2}$	$V_{\text{turb}}$ $\text{km s}^{-1}$
O VII	18.12	18.18	18.19	18.36–18.86	79–100
O VIII	18.12	18.19	17.93	17.42–18.47	46–111
C V	17.74	17.82	17.80	17.27–19.65	122–153
C VI	17.52	17.57	17.57	17.63–17.84	48–130

available for the strongest oscillator strength transition ( $1s^2 - 1s2p$ ) in C V, the column density and turbulent velocity could not be tightly constrained.  $1\sigma$  confidence limits were obtained of  $10^{15.91} - 10^{19.47} \text{ cm}^{-2}$  for column density and  $48 - 130 \text{ km s}^{-1}$  for turbulent velocity.

### 3.2.3 Nitrogen

The absorption lines of N VII prove more difficult to understand. Only one line is detected ( $\text{Ly}\alpha$ ) but by using an upper limit on the equivalent width of the undetected  $\text{Ly}\beta$  line a confidence region for column density and turbulent velocity can be determined. This region, however, does not agree with the region obtained by directly fitting a Voigt profile to the  $\text{Ly}\alpha$  line. A possible explanation for this is that the  $\text{Ly}\alpha$  line is not a single line but made up of several lines with a velocity separation greater than the turbulent width of the lines, but less than the instrumental resolution. Looking at the abundance of individual species in each zone of the DWA models presented in Turner et al. (2003) it is apparent that while other species have their column densities preferentially in one zone, N VII has its column density more evenly distributed between the zones. Considering the N VII  $\text{Ly}\alpha$  line to be made up of multiple lines from different zones brings the limit on column density into reasonable agreement with the predictions of the DWA models.

### 3.2.4 General

Table 2 compares the column densities and turbulent velocities derived above with those of the DWA models from Turner et al. (2003). As can be seen reasonable agreement is found between the values empirically derived here and those obtained by fitting DWA models to the data. Finally we compare the observed equivalent widths to the equivalent widths predicted by the DWA models. As can be seen from Fig. 6 a reasonable match is found although the observed absorption lines are found to be larger than predicted by a factor of  $\sim 1.25$ . This may be due to a combination of different species having different abundances than the assumed Solar abundance or the gas having a different turbulent velocity than the assumed  $100 \text{ km s}^{-1}$ . For example O VII requires an increase in abundance of  $\sim 3 - 5$  or an increase in turbulent velocity from  $100$  to  $\sim 130 \text{ km s}^{-1}$  to account for the  $\sim 1.25$  difference between observed and predicted equivalent widths.



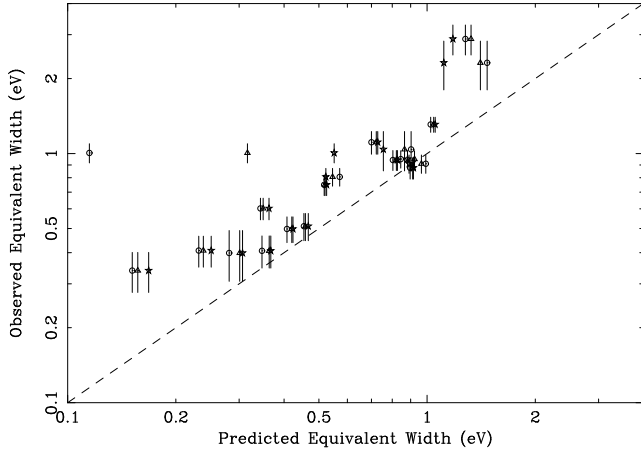


**Figure 6.** Comparison of equivalent widths for absorption lines between those observed and those predicted by the CLOUDY DWA models from Turner et al. (2003). Circles indicate model 1, triangles model 2 and stars model 3 from Turner et al. (2003). Only identified lines with accurate line details from Verner et al. (1996) are included.

#### 4 ABSORPTION BY DUST

The presence of dust in MCG–6-30-15 was first suggested by Reynolds et al. (1997) to explain the large Balmer decrement found in the optical spectrum. Lee et al. (2001) found that the drop in flux at  $\sim 0.7$  keV had the exact shape of absorption by Fe I and that the  $N_H$  implied by the discontinuity at the Fe I L-edge was consistent with that determined from  $E(V - B)$  reddening. This shape has also been seen in the Galactic black hole candidate Cygnus X-1 (Schulz et al. 2002). Lee et al. (2001) attributed this absorption to dust consisting of iron oxides or silicates (such as olivine) embedded in the warm absorber. However the sensitivity of the HETGS at the neutral oxygen edge was insufficient to measure the column of neutral oxygen accurately. Using RGS data Sako et al. (2003) produced an upper limit at 90 per cent confidence on O I column density of  $10^{16} \text{ cm}^{-2}$  using the apparent absence of a drop across the O I K-edge at 0.538 keV. Such a column density corresponds to a 0.5 per cent drop in flux across the O I edge.

Using our higher quality RGS data we have measured the drop in flux across the neutral O I edge. The 0.5–0.555 keV region was fitted to a power-law, Galactic absorption, the line profiles found in section 3 and an absorption edge at the O I edge energy. This produces an O I edge optical depth of 0.16–0.23 ( $1\sigma$ ) corresponding to a column density of  $10^{17.51} - 10^{17.67} \text{ cm}^{-2}$ . Given the column density of Fe I of  $10^{17.3} \text{ cm}^{-2}$  found in Turner et al. (2003), this suggests a neutral Fe:O ratio of  $\sim 1:2$ . This is consistent with the dust being in the form of iron oxides or silicates as found by Lee et al. (2001).

We repeated the above analysis on the 2000 data. Using 90 per cent confidence limits we find an optical depth at the edge of 0.13–0.34, consistent with the result found with the longer observation. As well as finding a different optical depth across the edge, the 90 per cent confidence limit range found here is an order of magnitude larger than that found by Sako et al. (2003) using the same data.

#### 5 LINE VARIABILITY

##### 5.1 Short timescale variations

To test for short term variability in the warm absorber the observation was split into two sets; one when the flux level was below a certain level and one when it was above that level. The level was set so an equal number of counts was present in each set. The level was found to be  $16.6 \text{ cts s}^{-1}$  for the 0.2–2 keV EPIC pn light-curve. The data from each set were then reduced using the method described in section 2.1. The best fitting continuum and line model from section 3 was fitted to each set of spectra separately and the errors for the best fitting parameters calculated as before. No significant change in position of the lines was found. Only 4 lines have a ratio of the equivalent widths from the high flux period to the low flux period which individually differs significantly from 1 (greater than  $2\sigma$ ; lines 20, 21, 36 and 46 corresponding to O I, O II, Fe XVII and Fe XXI with significances of  $3.0\sigma$ ,  $3.0\sigma$ ,  $4.8\sigma$  and  $2.0\sigma$  respectively). Given the large number of lines found, it is likely that random fluctuations would give false variability detections for one or two lines at a  $2\sigma$  threshold (the false alarm probability for 51 lines at  $2\sigma$  individually is  $\sim 0.4$ ). Since three of the lines have higher detection significances than this, the variability in these lines is likely to be real. Individually all other lines have a ratio that is consistent with 1. The variability in line strength can be used to estimate an upper limit for the distance between the warm absorbing region and the central source. Assuming that the increase in equivalent width is produced by recombination of more highly ionized species (brought about by the drop in continuum flux) then the recombination timescale,  $\tau_{\text{rec}} \lesssim \tau_{\text{obs}}$ , the timescale over which the spectrum is observed to change.  $\tau_{\text{obs}}$  is taken to be the average length of bright and dim time intervals, which is  $\sim 2500$  s. From Shull & van Steenberg (1982)

$$\tau_{\text{rec}} = \frac{A_{\text{rad}} T^{\chi_{\text{rad}}}}{n} \quad (1)$$

where  $T$  is the temperature of the gas,  $n$  is the density and  $A_{\text{rad}}$  and  $\chi_{\text{rad}}$  species dependant parameters. Using the definition of the ionization parameter used in Turner et al. (2003)

$$\xi = \frac{L_{2-10}}{nR^2} \quad (2)$$

then

$$\tau_{\text{rec}} = \frac{A_{\text{rad}} \xi R^2 T^{\chi_{\text{rad}}}}{L_{2-10}}. \quad (3)$$

Consequently, if  $\tau_{\text{rec}} \lesssim \tau_{\text{obs}}$  then

$$R \lesssim \sqrt{\frac{\tau_{\text{obs}} L_{2-10} A_{\text{rad}}}{\xi T^{\chi_{\text{rad}}}}}. \quad (4)$$

The O I and O II lines are produced solely in the low ionization zone. Taking the appropriate values for  $\xi$ ,  $L_{2-10}$ ,  $T$  from Turner et al. (2003) gives an upper limit of the radius of this zone as  $10^{19.5} \text{ cm}$ . Fe XVII and Fe XXI are found predominately in the highly ionized zones and using the appropriate values for this zone constrains it to lie within  $10^{17.0} \text{ cm}$  of the central source.

##### 5.2 Long timescale variations

To test the longer timescale variability in the warm absorber, the data from a previous observation of MCG–6-30-15 with *XMM-Newton* was extracted using the same process as described in Section 2.1. The line and continuum model of Section 3 was fitted to the data and the resulting parameters compared to the val-

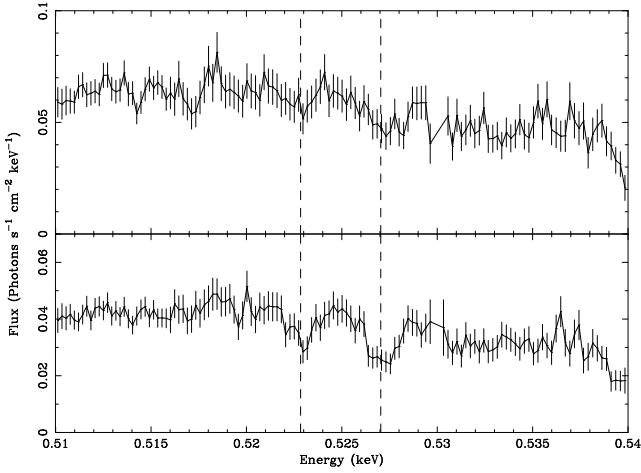


**Figure 7.** Detail of RGS spectra for high flux period (*upper*) and low flux period (*lower*). The dashed lines show the position of the O I and O II absorption lines. Their equivalent width is clearly higher during the low flux period.

ues obtained from the 2001 data analysed here. Because of the lower signal-to-noise ratio of the 2000 data not all the lines are found, so a comparison is only possible on the strongest lines. No lines appear to have statistically significant changes, possibly due to the poorer signal to noise in this data set. Examination of the spectra, however, reveals that several lines appear in the Branduardi-Raymont et al. (2001) spectrum but have fallen below a detectable level a year later. These lines occur at  $0.510715 \pm 0.0003$  and  $1.12631 \pm 0.001$  keV and are identified as Ca XIV and Fe XXIII respectively.

## 6 DISCUSSION

The analysis of the soft X-ray absorption lines of MCG–6–30–15 have revealed some interesting properties of the warm absorber. Most importantly the column densities measured for O VII and O VIII lines are large enough, when considered with Fe I, to account for the drop in flux at  $\sim 0.7$  keV. This means that the dominant effect on the shape of the soft X-ray spectrum of MCG–6–30–15 is from a dusty warm absorber. Any additional complexity from relativistically blurred emission lines is of low equivalent width.

The column densities and turbulent velocities that were measured for the other species agree with the predictions of the DWA model presented in Turner et al. (2003). The measured equivalent widths of the identified lines are larger than the predicted ones from the DWA models of Turner et al. (2003) but only by a factor of  $\sim 1.25$  which may be accounted for by a slightly higher than Solar abundance or higher than  $100 \text{ km s}^{-1}$  turbulent velocity in the warm absorbing gas than that assumed in the DWA models.

A broad range of ionization states is found for several elements, most notably oxygen and iron. This suggests the warm absorber consists of many zones with a range of ionization parameters as was assumed in Turner et al. (2003) or possibly a continuum of ionization parameter as suggested by Morales et al. (2000).

The variability of various absorption lines suggests that the most lowly and highly ionized gas is varying as the continuum flux varies. The increase in equivalent widths of these lines with decreasing flux is presumably from recombination of higher species in response to the drop in ionising flux. Using values for the re-

combination timescale upper limits can be placed on the distance of these two zones from the source of ionizing flux. The low ionization zone gas is found to lie within  $\sim 10$  pc of the central source whereas the highly ionized zone must lie very close to the central engine at  $10^{17}$  cm, at a similar distance as the BLR.

## ACKNOWLEDGMENTS

Based on observations obtained with *XMM-Newton*, an ESA science mission with instruments and contributions directly funded by ESA Member States and the USA (NASA). AKT acknowledges support from PPARC. ACF thanks the Royal Society for support. JCL thanks the Chandra fellowship for support. This was provided by NASA through the Chandra Postdoctoral Fellowship Award number PF2-30023 issued by the Chandra X-ray Observatory Center, which is operated by SAO for and on behalf of NASA under contract NAS8-39073.

## REFERENCES

- Arnaud K., 1996, in *Astronomical Society of the Pacific conference series*, Vol. 101, Jacoby G. H., Barnes J., ed, *Astronomical Data Analysis Software and Systems*, p. 17
- Ballantyne D. R., Ross R. R., Fabian A. C., 2002, *MNRAS*, 336, 867
- Ballantyne D. R., Weingartner J. C., Murray N., 2003, *A&A*, 409, 503
- Behar E., Kahn S. M., 2002, in *NASA Laboratory Astrophysics Workshop*, p. 23
- Behar E., Netzer H., 2002, *ApJ*, 570, 165
- Behar E., Sako M., Kahn S. M., 2001, *ApJ*, 563, 497
- Branduardi-Raymont G., Sako M., Kahn S. M., Brinkman A. C., Kaastra J. S., Page M. J., 2001, *A&A*, 365, L140
- Elvis M., Wilkes B. J., Lockman F. J., 1989, *ApJ*, 97, 777
- Fabian A. C., Vaughan S., 2003, *MNRAS*, 340, L28
- Fabian A. C. et al., 2002, *MNRAS*, 335, L1
- George I. M., Turner T. J., Netzer H., Nandra K., Mushotzky R. F., Yaqoob T., 1998, *ApJS*, 114, 73
- Lee J. C., Fabian A. C., Reynolds C. S., Brandt W. N., Iwasawa K., 2000, *MNRAS*, 318, 857
- Lee J. C., Iwasawa K., Houck J. C., Fabian A. C., Marshall H. L., Canizares C. R., 2002, *ApJ*, 570, L47
- Lee J. C., Ogle P. M., Canizares C. R., Marshall H. L., Schulz N. S., Morales R., Fabian A. C., Iwasawa K., 2001, *ApJ*, 554, L13
- McLaughlin B. M., Kirby K. P., 1998, *Journal of Physics B Atomic Molecular Physics*, 31, 4991
- Morales R., Fabian A. C., Reynolds C. S., 2000, *MNRAS*, 315, 149
- Nicastro F., Fiore F., Matt G., 1999, *ApJ*, 517, 108
- Otani C. et al., 1996, *PASJ*, 48, 211
- Pradhan A. K., Chen G. X., Delahaye F., Nahar S. N., Oelgoetz J., 2003, *MNRAS*, 341, 1268
- Press W. H., Teukolsky S. A., Vetterling W. T., Flannery B. P., 1999, *Numerical Recipes in C*. Cambridge University Press, p. 113
- Rózańska A., Dumont A.-M., Czerny B., Collin S., 2002, *MNRAS*, 332, 799
- Reynolds C. S., 1997, *MNRAS*, 286, 513

- Reynolds C. S., Ward M. J., Fabian A. C., Celotti A., 1997, MNRAS, 291, 403
- Sako M. et al., 2001, A&A, 365, L168
- Sako M. et al., 2003, ApJ, 596, 114
- Schulz N. S., Cui W., Canizares C. R., Marshall H. L., Lee J. C., Miller J. M., Lewin W. H. G., 2002, ApJ, 565, 1141
- Shih D. C., Iwasawa K., Fabian A. C., 2002, MNRAS, 333, 687
- Shull J. M., van Steenberg M., 1982, ApJS, 48, 95
- Turner A. K., Fabian A. C., Vaughan S., Lee J. C., 2003, MNRAS, 346, 833
- Vaughan S., Edelson R., 2001, ApJ, 548, 694
- Verner D. A., Verner E. M., Ferland G. J., 1996, Atomic Data and Nuclear Data Tables, 64, 1